Molecular Therapy
Nucleic Acids
Original Article

Smart exosomes with lymph node homing and immune-amplifying capacities for enhanced immunotherapy of metastatic breast cancer

Panpan Ji,[1,6] Zheng Yang,[2,6] Hua Li,[3,6] Mengying Wei,[4] Guodong Yang,[4] Helin Xing,[5] and Qiuyun Li[1]

[1]Department of Breast Surgery, Guangxi Medical University Cancer Hospital, Nanning, Guangxi 530021, China; [2]Department of Plastic Surgery, The First Medical Center, Chinese PLA General Hospital, Beijing 100853, China; [3]Shaanxi Provincial Center for Disease Control and Prevention, Xi'an, Shaanxi 710054, China; [4]The State Laboratory of Cancer Biology, Department of Biochemistry and Molecular Biology, Fourth Military Medical University, No. 169 Changlexi Road, Xi'an, Shaanxi 710032, China; [5]Department of Prosthodontics, Beijing Stomatological Hospital and School of Stomatology, Capital Medical University, NO. 4 Tiantanxi Road, Beijing 100050, China

Tumor-draining lymph nodes (TDLNs) are the primary sites to initiate immune responses against cancer, as well as the origin of metastasis for most breast cancer cases. Reverting the immunosuppression microenvironment in TDLNs is critical to improving the outcome of the malignancy, though still a big technical challenge. In this study, a type of smart exosomes was developed in which the exosome surface was functionally engineered with CD62L (L-selectin, a gene for lymphocyte homing to lymph nodes) and OX40L (CD134L, a gene for effector T cell expansion and regulatory T cell [Treg] inhibition) by forced expression of the genes in the donor cells. Compared with control exosomes, the smart exosomes displayed strong TDLN homing capacity in the 4T1 syngeneic mouse model. Moreover, injection of the smart exosomes activated effector T cells and inhibited Treg induction, thereby amplifying the antitumor immune response and inhibiting tumor development. Together, the engineered smart exosomes provide a novel nanoplatform for TDLN-targeted delivery and cancer immunotherapy.

INTRODUCTION

Breast cancer is the leading cause of cancer-related deaths among females around the world,[1,2] and 40% of breast cancer cases will progress to metastasis.[3,4] Immunotherapy holds promise for cancer therapy. Tumor-infiltrating lymphocytes are emerging as one of the key players in the tumor microenvironment.[5] The majority of tumor-infiltrating lymphocytes are T cells that can be divided into $CD4^+$ helper cells, regulatory T cells (Tregs), and $CD8^+$ T cells.[6] Tregs with a $CD4^+$, $CD25^+$, $Foxp3^+$ phenotype can inhibit the activation and proliferation of $CD8^+$ T cells and $CD4^+$ T cells. High numbers of Tregs are associated with a worse prognosis in breast cancer. Specific activation of the tumor immunity is the key for cancer immunotherapy. Tumor-draining lymph node (TDLN) metastasis is the most common type for breast cancer.[7,8] Moreover, TDLNs are the primary immune organs for cancer immunity, where the tumor antigens and leukocytes are first drained.[9] Accumulating evidence implicates that cancer-derived immune-suppressive factors privilege TDLNs, enabling tumors to invade and metastasize.[10] Activation of antitumor immune response specifically in the lymph nodes is of great promise in cancer immunotherapy.

Recently, targeted delivery of immune-activating drugs to TDLNs for systemic antitumor enhancement has been intensively studied.[11–13] For example, Ding and colleagues have developed a DNA-based nanodevice to boost robust tumor-specific immune response in TDLNs,[14] suggesting that rational design of nanocarriers for enhanced immune responses in TDLNs holds great promise for cancer immunotherapy. Nanostructures with reasonable size and shape are essential for efficient TDLN delivery. Exosomes are 30- to 150-nm vehicles that are functionally involved in many pathophysiological processes, such as antigen presentation, immune response, inflammation, cardiovascular disease, and cancer.[15–19] Because of the bilayer membrane structure, naturally biocompatible characteristics, and nano-scale size, exosomes have been widely used as drug delivery vesicles.[20] Moreover, exosomes could be easily engineered for improved drug loading and tissue-specific targeting.[21–25] Thus, exosomes are promising natural nanocarriers for TDLN-targeted delivery.

CD62L (also called L-selectin), which is a vascular adhesion molecule constitutively expressed on lymphocytes, is a type I transmembrane protein directing leukocyte migration and homing to lymph nodes.[26] In addition, OX40/OX40L signals play an important role in promoting T cell immunity.[27–29] OX40/OX40L signal is involved in effector

Received 14 May 2021; accepted 5 October 2021;
https://doi.org/10.1016/j.omtn.2021.10.009.

[6]These authors contributed equally

Correspondence: Qiuyun Li, Department of Breast Surgery, Guangxi Medical University Cancer Hospital, No.71 Hedi Road, Nanning, Guangxi 530021, China.
E-mail: qyli1020@sina.com
Correspondence: Helin Xing, Department of Prosthodontics, Beijing Stomatological Hospital and School of Stomatology, Capital Medical University, NO. 4 Tiantanxi Road, Beijing 100050, China.
E-mail: xinghelin110@163.com
Correspondence: Guodong Yang, The State Laboratory of Cancer Biology, Department of Biochemistry and Molecular Biology, Fourth Military Medical University, No. 169 Changlexi Road, Xi'an, Shaanxi 710032, China.
E-mail: yanggd@fmmu.edu.cn

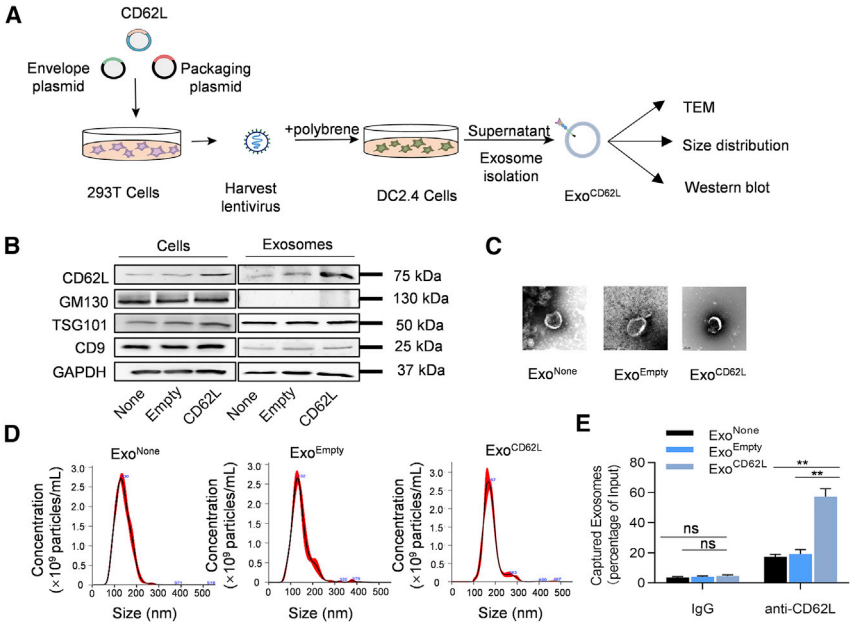

Figure 1. Construction and characterization of Exo^{CD62L}

(A) Schematic representation of the experimental procedure. CD62L-overexpressing lentivirus was packaged. DC2.4 cells as exosome donor cells were then infected with the lentivirus, followed by exosome isolation and characterization. (B) Western blot analysis of the expression of CD62L and inclusive and exclusive exosomal markers in both the parental cells and derived exosomes. Representative data of three different experiments. (C) Transmission electron microscopy (TEM) analysis of Exo^{CD62L}. (D) Size distribution of the indicated exosomes was analyzed by NanoSight. (E) Nanoparticle tracking analysis of the captured exosomes by anti-CD62L antibody. **P<0.01 by one-way ANOVA. ns, no significance.

T cell expansion and survival. OX40/OX40L interaction also reduces Foxp3 expression and abolishes the suppressive activity of Tregs, which are immunosuppressive and can inhibit or downregulate the induction and proliferation of effector T cells.[30] Together, it is reasonable to deduce that engineering of the exosomes with CD62L and OX40L would be a promising strategy to activate the cancer immunity in TDLNs.

In this study, we describe a strategy utilizing exosomes as a TDLN-targeted delivery platform to provoke a robust tumor-specific immune response for cancer therapy. The engineered smart exosomes with OX40L and CD62L simultaneously displayed on the surface have potent efficacy in TDLN targeting and thus tumor immunotherapy augmentation.

RESULTS

Construction and characterization of Exo^{CD62L}

To display CD62L on the exosomal surface, exosome donor DC2.4 cells infected with lentivirus overexpressing CD62L were cultured in serum-free medium (Figure 1A). DC2.4 cells with no infection or infected with control virus served as controls. qPCR and western blot analysis confirmed overexpression efficiency in the donor cells (Figure 1B; Figure S1). After 48-h culture, exosomes were isolated by ultracentrifugation and designated as Exo^{None}, Exo^{Empty}, and Exo^{CD62L}, respectively. Western blot analysis of the inclusive and exclusive exosomal markers suggested the exosomal identity of isolated extracellular particles (Figure 1B). Transmission electron microscopy (TEM) and nanoparticle tracking analysis (NTA) further confirmed the exosomal size and morphology of the isolated extracellular vesicles. Notably, CD62L overexpression had nearly no significant effects on the expression of markers, size, and morphology of exosomes (Figures 1B–1D). In order to further confirm the exosomal surface expression of CD62L, exosomes were captured by CD62L antibody. As expected, CD62L antibody captured the exosomes efficiently, indicating that CD62L was efficiently loaded onto the exosomal surface (Figure 1E).

Enhanced lymph node homing of Exo^{CD62L}

To explore whether CD62L-engineered exosomes (Exo^{CD62L}) had lymph node targeting capacity, Exo^{None}, Exo^{Empty}, and Exo^{CD62L} labeled with DiR or DiI were subcutaneously injected into 4T1 breast tumor-bearing BALB/c mice. *Ex vivo* imaging analysis showed that there were more Exo^{CD62L} accumulated in lymph nodes in comparison with Exo^{None} and Exo^{Empty} (Figures 2A and 2B). In contrast, no obvious difference of fluorescence intensity was found in spleen, liver, heart, lung, and kidney (Figure 2A). Fluorescence microscope analysis further revealed a similar distribution profile in lymph node, tumor, and other organs (Figures S2 and S3). To further validate the targeting efficiency of the engineered exosomes in lymph nodes, mice were injected with Exo^{None}, Exo^{Empty}, and Exo^{CD62L} loaded with equal amounts of *cel*-miR-54, a microRNA (miRNA) with no homolog in human or mouse (Figure 2C). Compared to the control groups, *cel*-miR-54 levels in lymph nodes were higher in Exo^{CD62L}-treated mice (Figure 2D). Notably, abundance of *cel*-miR-54 was also found to be much higher in tumor and spleen in mice with Exo^{CD62L} treatment (Figure S4). The above research proved that Exo^{CD62L} efficiently targeted to lymph nodes and tumors.

To further explore whether the increased Exo^{CD62L} in TDLNs was attributed to interaction with the lymphatic endothelial cells (LECs) in lymph nodes, colocalization of the labeled exosomes and LECs was observed by immunofluorescent microscope analysis. As shown in Figure S5, there was much more co-localization between LECs and Exo^{CD62L} compared with the control Exo^{None} and Exo^{Empty}. Accordingly, within the lymph nodes, there were also more Exo^{CD62L} colocalized with CD3$^+$ cells and Foxp3$^+$ cells than control Exo^{None} and Exo^{Empty} (Figures 2E–2H). Together, all data confirmed that Exo^{CD62L} could effectively target TDLNs via enhanced interaction with LECs.

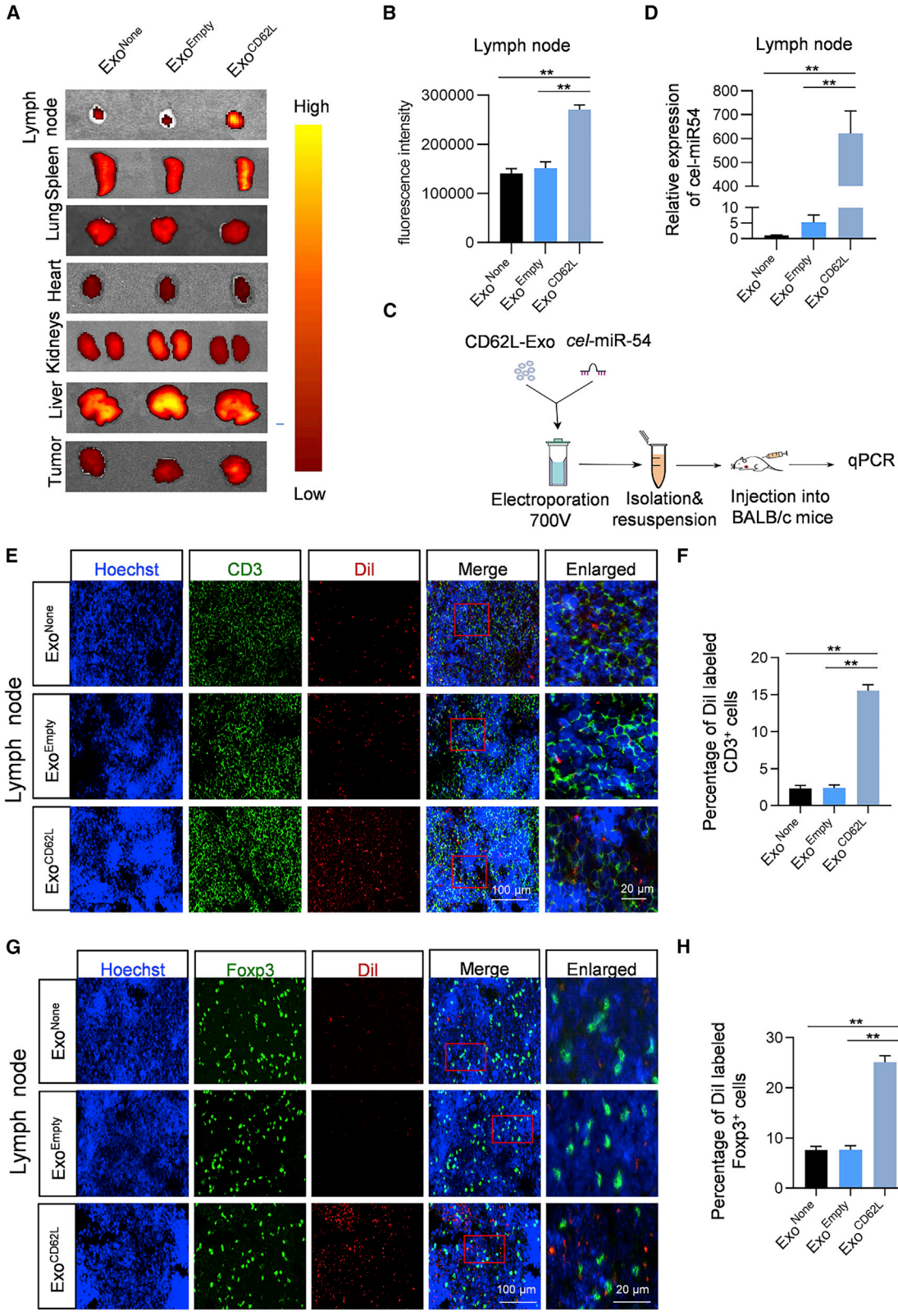

(legend on next page)

Exo^{Smart} promotes effector T cell expansion and inhibits Treg induction

To stimulate the immune response in TDLNs, OX40L was engineered on the exosomal surface. Similar to the construction of Exo^{CD62L}, exosomes with OX40L displayed on the surface were isolated from DC2.4 cells infected with OX40L-overexpressing lentivirus (Figures 3A and 3B; Figure S6). Western blot analysis, TEM, and NTA confirmed the identity of the exosomes, and overexpressing OX40L had no effects on exosome identity, size, morphology, and yield (Figures 3B–3D). The exosome capture experiment further confirmed that OX40L protein was efficiently expressed on the exosomal surface (Figure 3E).

In the following experiments, exosomes with CD62L and OX40L simultaneously displayed on the surface were engineered (Exo^{Smart}) by co-expressing the two genes in donor cells (Figure 4A). We assumed that Exo^{Smart} can target the TDLNs and reverse the tumor-suppressive immune microenvironment in/beyond the TDLNs. To this end, 4T1 breast tumor-bearing mice were subcutaneously injected with 200 μg of Exo^{None}, Exo^{Ctrl}, or Exo^{Smart} (Figure 4B). Compared with two control exosomes, Exo^{Smart} treatment significantly promoted CD3$^+$ cell proliferation, as seen by more Ki67-positive cells in the TDLNs from Exo^{Smart}-treated mice (Figure 4C; Figure S7A). Flow cytometry analysis further confirmed that the ratio of CD8$^+$ cytotoxic lymphocytes (CTLs) and helper T cells in TDLNs was much higher in Exo^{Smart}-treated mice (Figures 4E and 4F). In contrast, the number of Ki67$^+$ Foxp3$^+$ cells (proliferating Tregs) was significantly lower in the TDLNs from Exo^{Smart}-treated mice (Figures 4D and 4G; Figure S7B). In accordance with the findings in TDLNs, enhanced effector T cell expansion and inhibited Treg induction were also observed in tumor tissues (Figure S8). With the inhibited Treg and promoted effector T cell function, the proinflammatory cytokines interleukin-2 (IL-2) and interferon (IFN)-γ, which promote antitumor immune response, were found significantly enhanced in both the TDLNs and tumor tissues after Exo^{Smart} treatment (Figure 4H; Figure S9A). In contrast, expression of the immune-suppressive IL-10, Foxp3, and transforming growth factor-β (TGF-β) were obviously decreased in both lymph nodes and tumors after Exo^{Smart} treatment (Figure 4I; Figure S9B). All data suggested that Exo^{Smart} can inhibit Treg induction and promote effector T cell expansion in TDLNs and beyond.

Immunotherapy effects of Exo^{Smart} in 4T1 syngeneic mouse model

In the following experiments, we investigated the therapeutic effects of Exo^{Smart} in a 4T1 syngeneic mouse model. To monitor metastasis, 4T1-Luc2 cells were injected into the right breast pads. When the tumor reached the size of ~70 mm^3 (over 7 days after tumor transplantation), the mice were administrated with Exo^{None}, Exo^{Ctrl}, or Exo^{Smart} every other day for four times (Figure 5A). As expected, there were fewer lymph nodes with metastasis of the cancer cells observed in the Exo^{Smart} treatment group in comparison with the control treatments, indicating that Exo^{Smart} significantly inhibited the spontaneous lymph node metastasis (Figures 5B and 5C). In accordance with the decreased ratio of metastasis, Exo^{Smart} treatment significantly suppressed the growth of tumor and prolonged the mouse survival rate (Figures 5D and 5E). Together, all these data convinced us that Exo^{Smart} had potent efficiency in inhibition of metastatic breast cancer via activating cancer immunity in TDLNs and beyond.

DISCUSSION

TDLNs are the priming sites of antitumor immunity, and immune escape in the TDLNs is the important reason for tumor metastasis.[31,32] In this study, we repurposed exosomes for nanotherapeutics reverting the immunosuppressive microenvironment in TDLNs, which potently activate tumor immunity and inhibit growth and metastasis in the 4T1 syngeneic mouse model.

Therapeutic delivery of antigens or immune adjuvants via nanoparticles to TDLNs is of great importance for cancer immunotherapy. Growing evidence demonstrates that the delivery efficiency largely depends on the size of the particles.[33] In addition, delivery efficiency is also affected by the biocompatibility of nanomedicines.[34,35] As expected, we here confirmed that exosomes are ideal carriers for targeted delivery to TDLNs, which is at least partially attributed to their high biocompatibility and appropriate particle size. The immunosuppressive tumor microenvironment in either TDLNs or the tumor region is now recognized as a critical element for breast cancer development and progression.[36,37] Immunotherapy strategies aimed at reshaping antitumor immune microenvironment are emerging as the most hopeful therapy for advanced cancer. Recently, checkpoint blockade therapies, such as anti-PD-1 and anti-CTLA-4,[38] showed success in promoting antitumor immune responses of certain cancers.[39,40] Chimeric antigen receptor T cell immunotherapy is another promising strategy for tumor immunotherapy,[41] although identification of cancer-specific antigens remains a big challenge.[42] Notably, most solid tumors remain poorly responsive to the two existing immunotherapies, mainly because of the low infiltration of the therapeutics.[39] The advantages of our strategy mainly include the following: (1) Exosomes are native nanovesicles with high penetration for nearly all the biological barriers, allowing

Figure 2. Enhanced lymph node homing of *Cd62l*-engineered exosomes

(A) *Ex vivo* fluorescence imaging analysis of the distribution of the DiR-labeled exosomes in different organs. Mice were injected with the indicated DiR-labeled exosomes. Twenty-four hours later, the lymph node, spleen, lung heart, kidneys, liver, and tumor were harvested for *ex vivo* imaging analysis. Data shown are representative of 3 mice in each group. (B) Statistical analysis of the fluorescence intensity in lymph nodes from mice treated with controls or Exo^{CD62L} as indicated. n = 3. **p < 0.01 by one-way ANOVA. (C) Schematic illustration of the experimental procedure. Mice were injected with exosomes loaded with *cel*-miR-54. Twenty-four hours after injection, *cel*-miR-54 levels in lymph nodes were examined by qPCR. (D) Expression of *cel*-miR-54 in lymph nodes from mice treated with controls or Exo^{CD62L} as indicated. Data are presented as mean ± SEM of three different experiments. **p < 0.01 by one-way ANOVA. (E) Representative immunofluorescence images showing the co-localization of the exosomes (red) and CD3$^+$ T cells (green) in the lymph node. (F) Statistical analysis of (E). n = 3. **p < 0.01 by one-way ANOVA. (G) Representative immunofluorescence images showing the co-localization of the exosomes (red) and Foxp3$^+$ T cells (green) in the lymph node. (H) Statistical analysis of (G). n = 3. **p < 0.01 by one-way ANOVA.

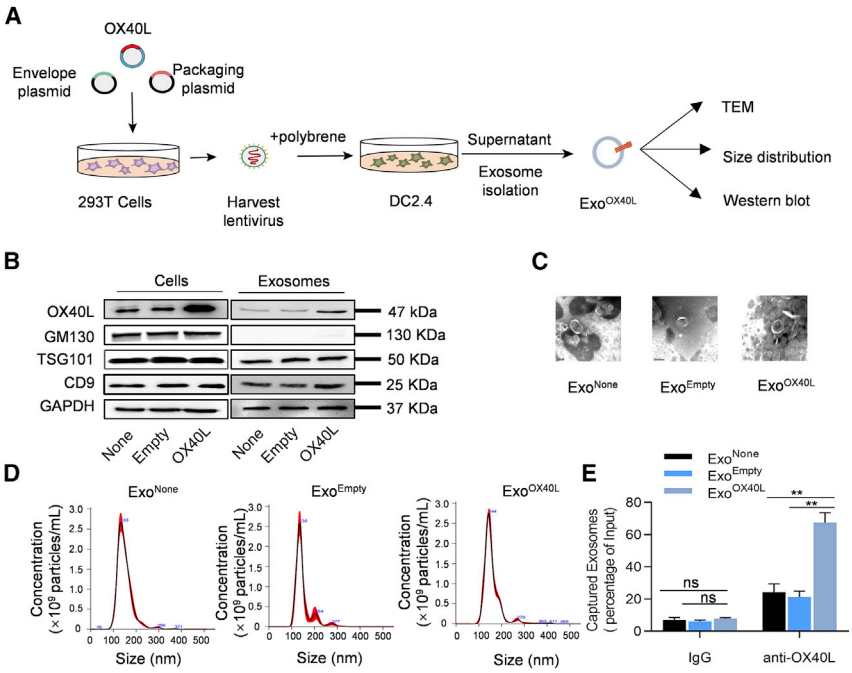

Figure 3. Construction and characterization of Exo^{OX40L}

(A) Schematic representation of the experimental procedure. OX40L-overexpressing lentivirus was packaged. DC2.4 cells as exosome donor cells were then infected with the lentivirus, followed by exosome isolation and characterization. (B) Western blot analysis of the expression of OX40L and inclusive and exclusive exosomal markers in both the parental cells and derived exosomes. Representative data of three different experiments. (C) Transmission electron microscopy (TEM) analysis of Exo^{OX40L}. (D) Size distribution of the indicated exosomes was analyzed by NanoSight. (E) Nanoparticle tracking analysis of the captured exosomes by anti-OX40L antibody. **P<0.01 by one-way ANOVA. ns, no significance.

them to highly accumulate in the targeted tissues. The size range of exosomes allows them to be a natural carrier for TDLNs. To increase the TDLN targeting efficiency, CD62L was engineered on the surface. CD62L is essential for naive lymphocytes homing to high endothelial venule (HEV)-bearing secondary lymphoid organs.[43] HEVs are specialized for lymphocyte recruitment in secondary lymphoid organs such as lymph nodes. Moreover, HEVs have also been observed in solid tumors, which correlated with lymphocyte infiltration and immune orientation.[44–46] CD62L on lymphocytes serves as a primary adhesion receptor when the cells are tethering and rolling along the apical aspects of HEVs.[47–49] (2) Exosomes are native immune modulators. Exosomes have been found to interact and fine-tune the function of immune cells *in vivo* by amplifying immunomodulatory effects or integrating the synergistic effect of different molecules.[15,50] (3) OX40L on the exosomal surface is a potent immune agonist of super advantages. OX40-OX40L interaction-mediated immune activation is applicable to nearly all cancers. The OX40-OX40L pathway plays an important role in a variety of pathophysiological processes between T cells, lymphocytes, and non-lymphocytes.[27–29] Enhanced activation of the OX40/OX40L system amplifies and prolongs the immune reaction via various mechanisms.[51–54] Of note, accumulation of Tregs results in immune paralysis, and inactivation of Tregs is a major goal for cancer immunotherapy. CTLA4 blockade not only activates $CD4^+$ T cells but also increases the number of Tregs,[55] limiting the therapeutic efficacy. Zhang et al. showed that OX40-OX40L interactions inhibit Foxp3 and Tregs via upregulation of BATF3.[29] Consistently, our study revealed that OX40L-engineered exosomes had excellent Treg inhibition function. Together, it is highly reasonable to conclude that the CD62L/OX40L-engineered exosomes could be an attractive off-the-shelf immunotherapy for pan-cancers.

In this study, CD62L and OX40L were engineered on the exosomal surface mainly based on gene transfection in the donor cell, a widely used method in the field. Frankly, the strategy is time consuming and difficult for translational application. Recently, CP05, a CD63-specific exosomal anchor peptide, has been shown to have a promising potential for exosome engineering and targeted therapeutic drug delivery.[56] It is thus reasonable to deduce that coating of the exosomes with CP05-conjugated CD62L and OX40L functional domains might be an alternative strategy. Moreover, enrichment of CD62L and OX40L in exosomes in our study is limited, and the activity for tissue targeting and immune activation is relatively weak, though statistically significant. Further improving the membrane protein expression on the exosomes would increase the targeting and therapeutic effects. It is worthwhile to explore whether exosomes anchored with CP05-functional CD62L/OX40L domain could have stronger effects. It is also important to note that CD62L and OX40L are transmembrane proteins and their interaction with corresponding receptors on the recipient cell membrane is an important basis for function. In other words, the two molecules on the exosomal surface, rather than endocytosed by the recipient cells, are prerequisite for their function. Further studies to avoid their uptake by the lymphocytes in TDLNs would further augment the function of the smart exosomes.

Collectively, our findings highlight the promising application of activating immunological reaction in lymph nodes with the proposed CD62L- and OX40-engineered exosomes. Further studies need to be conducted to optimize the doses, size range, and origin of exosomes toward higher efficacy.

MATERIALS AND METHODS

Cell culture

HEK293T cells and 4T1-Luc2 cells were purchased from ATCC. DC2.4 cells were purchased from FuHeng Cell Center. HEK293T cells

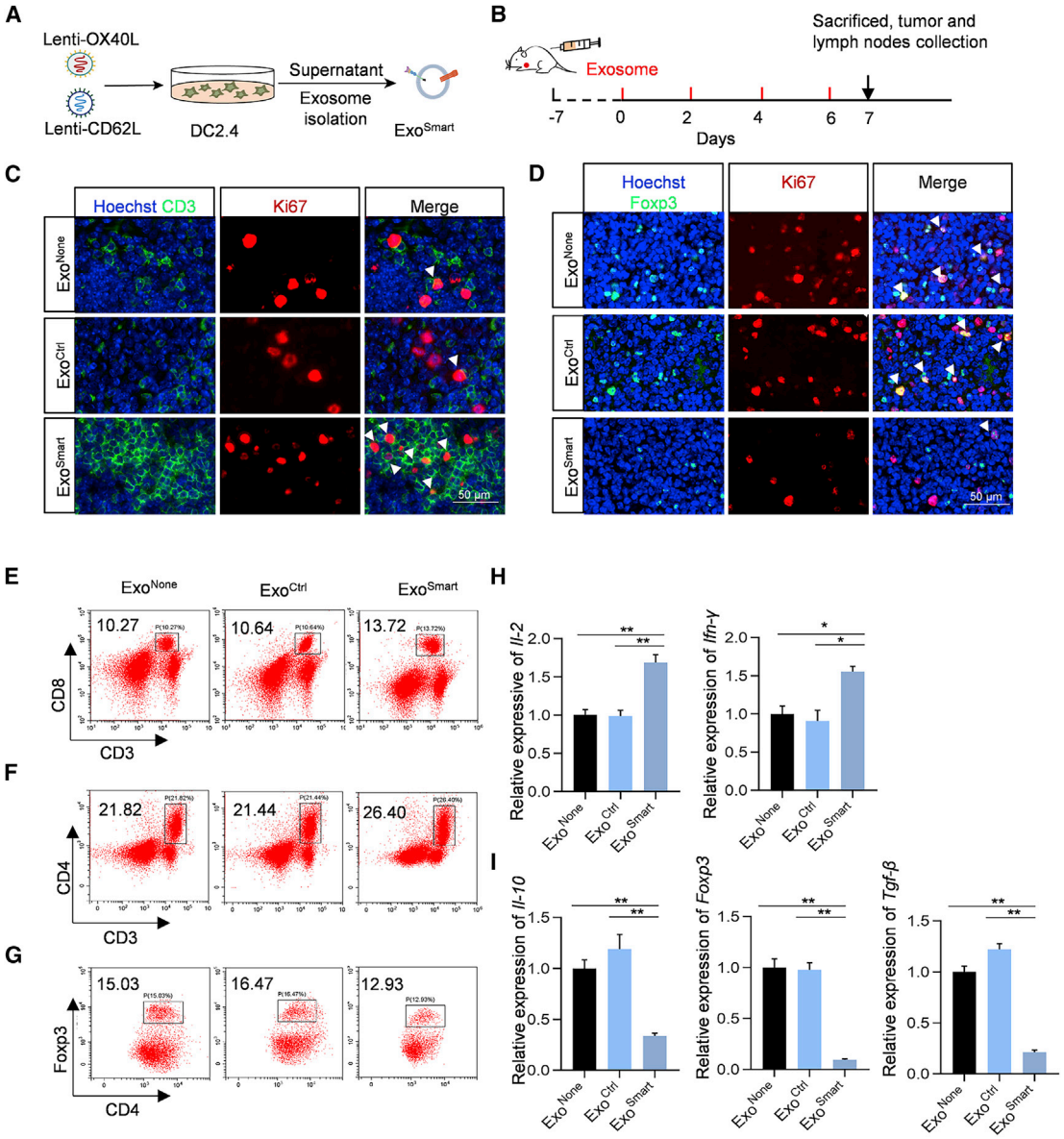

Figure 4. Exo^{Smart} promotes effector T cell activation and inhibits Tregs in lymph nodes simultaneously

(A) Experimental procedure for Exo^{Smart}. Donor cells were forced expressed with CD62L and OX40L by infection of the overexpressing lentivirus. (B) Schematic representation of the exosome treatment. 4T1 breast tumor-bearing mice were injected with the exosomes at the indicated time. (C) Representative images of immunostaining of Ki67 (red) and CD3 (green) in lymph nodes from mice with indicated treatments. n = 3. (D) Representative images of immunostaining of Ki67 (red) and Foxp3 (green) in lymph nodes from mice with indicated treatments. n = 3. (E) Representative flow cytometric analysis of CTL ($CD3^+CD8^+$ T cells) in lymph nodes from mice with indicated treatments. (F) Representative flow cytometric analysis of $CD4^+$ helper cells ($CD3^+CD4^+$ T cells) in lymph nodes from mice with indicated treatments. (G) Representative flow cytometric analysis of Tregs ($CD3^+CD4^+Foxp3^+$ T cells) in lymph nodes from mice with indicated treatments. (H) qPCR analysis of the expression of IL-2 and IFN-γ in lymph nodes from mice with indicated treatments. (I) qPCR analysis of the expression of IL-10, Foxp3, and TGF-β detected in lymph nodes from mice with indicated treatments. Data are representative of three different experiments and expressed as mean ± SEM. *$p < 0.05$, **$p < 0.01$ by one-way ANOVA.

were cultured in DMEM (HyClone, Logan, UT, USA) supplemented with 10% heat-inactivated fetal bovine serum (FBS) (HyClone, Logan, UT, USA) and 1% penicillin-streptomycin (HyClone, Logan, UT, USA). DC 2.4 cells and 4T1-Luc2 cells were cultured in RPMI-1640 (HyClone, Logan, UT, USA) supplemented with 10% heat-inactivated FBS (HyClone, Logan, UT, USA) and 1% penicillin-streptomycin (HyClone, Logan, UT, USA). All cells were maintained at 37°C in 5% CO_2.

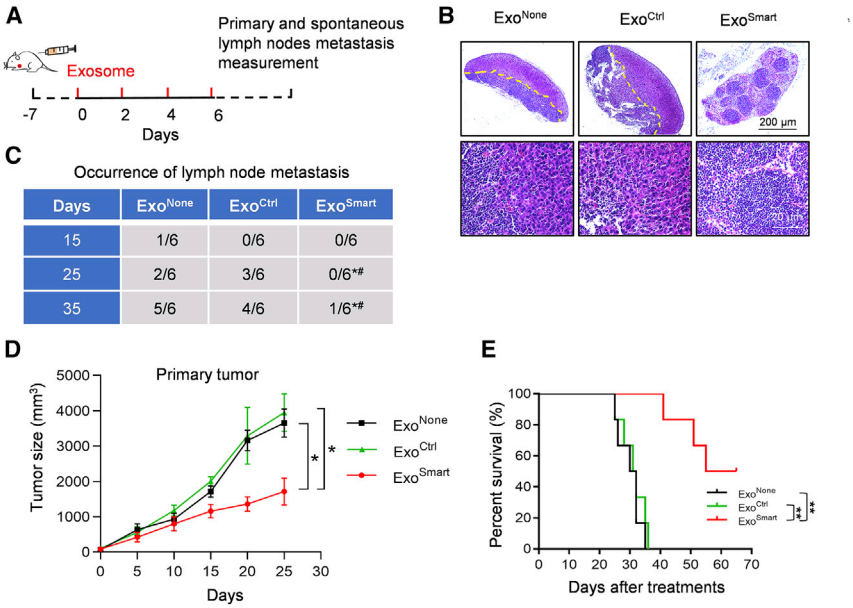

Figure 5. Therapeutic effects of Exo^{Smart} on survival and tumor metastasis

(A) Exosome injection schedule. (B) Representative H&E staining of the lymph node sections from mice with indicated treatments. Mice were sacrificed on day 25. n = 6. (C) Numbers of lymph node metastases from tumor-bearing mice treated as indicated. Mice were sacrificed on day 25. n = 6 mice per group. *p < 0.05 versus Exo^{None}, #p < 0.05 versus Exo^{Ctrl}. (D) Tumor growth in mice treated with indicated exosomes. Tumor size was monitored every 5 days. Data are expressed as mean ± SEM; n = 6. (E) Survival curves of tumor-bearing mice treated with indicated exosomes. n = 6 mice per group. **p < 0.01 by log rank test.

Plasmid construction and lentivirus package

Genes encoding OX40L and CD62L were synthesized by GenScript (Nanjing, China) and cloned into pCDH-CMV-MCS-EF1-Puro with BamHI and EcoRI. The resultant correct plasmids were designated as pCDH-CMV-OX40L-EF1-Puro and pCDH-CMV-CD62L-EF1-Puro, respectively.

pCDH-CMV-OX40L-EF1-Puro or pCDH-CMV-CD62L-EF1-Puro was transfected into HEK293T cells together with psPAX2 and pMD2G at the ratio of 4:3:1 by HighGene transfection (ABclonal) as instructed. Briefly, the three plasmids dissolved in FBS-free DMEM medium were mixed with HighGene transfection reagent and incubated at room temperature for 25 min. Then, 293T cells at 70%–80% confluence received the transfection, and the medium was changed with fresh 10% FBS-containing medium 6 h later. Lentivirus particles were collected from the medium supernatant filtered through a 0.45-μm filter (Millipore) 48 h post transfection. For lentivirus infection, DC2.4 cells were incubated with the lentiviruses at MOI of 50 in the presence of 8 $\mu g \cdot mL^{-1}$ polybrene (Sigma, St. Louis, MO, USA). Positive cells were selected by puromycin at 10 $\mu g \cdot mL^{-1}$.

Exosome isolation and characterization

Exosomes from control or OX40L- or CD62L-overexpressing cells were isolated by ultracentrifugation. Briefly, cells infected with the indicated lentivirus were cultured with serum-free medium, and the cell culture medium was centrifuged at 3,000 × *g* for 15 min to remove cells and eliminate cellular debris. Next, the supernatant was centrifuged at 100,000 × *g* for 2 h to obtain the exosomes. After isolation, all the exosomes were resuspended in PBS and stored at −80°C.

The size distribution of the isolated exosomes was analyzed by NanoSight (Malvern, UK). The morphology of isolated exosomes was analyzed by TEM. Briefly, the exosomes were added onto the grid and stained with 2% uranyl acetate. The images were analyzed by an electron microscope (JEM-2000EX TEM; JEOL, Tokyo, Japan).

Animal housing and tumor inoculation

BALB/C female mice (6–8 weeks and weighing 20–25 g) were obtained from the Lab Animal Center of the Fourth Military Medical University. The mice were housed 3–5 per cage under specific pathogen-free conditions in a 12-h light/dark cycle with food and water *ad libitum*. The experiments were approved by the Institutional Animal Experiment Administration Committee of the Fourth Military Medical University (REF NO.20200426).

The 4T1 syngeneic mouse model was established by implanting 5 × 10^5 4T1-Luc2 cancer cells in 100 μL of PBS into the right second mammary fat pads of the BALB/c mice. Tumor growth was monitored by palpation every 5 days. Tumor size was calculated as V = a × $b^2/2$, where a indicates the longer diameter and b indicates the shorter diameter.

Exosome labeling and *in vivo* fluorescence tracing of exosomes

Exosomes (1 μg/μL) were labeled with DiI (1,1′-Dioctadecyl-3,3,3′,3′-tetramethylindocarbocyanine perchlorate) or DiR (1,1'-Dioctadecyl-3,3,3',3'-tetramethylindotricarbocyanine iodide) by incubation with the dyes (1 mM) at the ratio of 500:1 in volume for 5 min at 37°C. The free dye was removed by additional exosome isolation with ultracentrifugation.

For *in vivo* tracing of exosomes, mice were subcutaneously injected with 200 μg of the indicated DiR-labeled exosomes. The localization of the exosomes in different organs was detected by imaging with the IVIS Lumina II *in vivo* imaging system (PerkinElmer, Thermo Fisher, USA).

To visualize the location of exosomes in TDLNs and other tissues, the DiI-labeled exosomes were injected. The colocalization between DiI signals and cell markers (stained with corresponding antibodies) was examined under a Nikon A1 Spectral Confocal Microscope (Nikon, Japan).

cel-miR-54 loading into exosomes

Exosomes at a protein concentration of 1 mg/mL (BCA Protein Assay Kit, Thermo Scientific) were electroporated with 1 OD *cel*-miR-54 mimics (GenePharma, Shanghai) at 700 V/150 mF in 0.4-cm-wide electroporation cuvettes. Sequences for *cel*-miR-54 are listed in Table S1. Subsequently, exosomes were treated with RNase and washed with cold PBS, followed by isolation with ultracentrifugation to remove the free nucleic acids.

Real-time polymerase chain reaction

Total RNA was isolated with TRIzol according to the manufacturer's instructions (Invitrogen, USA). Reverse transcription was conducted with the PrimeScript First-Strand cDNA Synthesis Kit (Takara, China) for analysis of mRNA expression. miRNAs were reverse-transcribed with the miRcute First-Strand cDNA Synthesis Kit (Tiangen Biotech, China). Subsequently, qPCR reactions (20 μL) were performed by FastStart Essential DNA Green Master. The primers for *Ox40l*, *Cd62l*, *Il-2*, *Il-10*, *Tgf-β*, *Foxp3*, *Inf-γ*, and *Gapdh* used in this study are listed in Table S1. The mRNA expression was normalized to *Gapdh*, and miRNA expression was normalized to *U6b*. Relative expression was calculated with the $2^{-\Delta\Delta Ct}$ (the delta delta CT value for each set of samples for each target gene relative to the endogenous control) method.

Western blot

Total protein of the donor cells or isolated exosomes was extracted with RIPA Lysis Buffer (Beyotime Biotechnology, China) at 4°C for 30 min. Protein concentration was determined by BCA Protein Assay (Thermo Scientific, Somerset, NJ). Proteins were then concentrated on SDS-PAGE (6%) and separated by SDS-PAGE (12%) and transferred to Nitrocellulose membranes. After blocking with 3% bovine serum albumin (BSA), the membranes were subsequently incubated with first antibodies anti-OX40L (ab229021, Abcam), anti-CD62L (ab253241, Abcam), anti-GM130 (11308-1-AP, ProteinTech), anti-TSG101 (ab83, Abcam), anti-CD9 (ab92726, Abcam), and anti-GAPDH (D110016-0100, BBI Life Sciences) at 4°C for 12 h. After being washed three times in TBST (Tris buffered saline with tween-20), the membranes were incubated with the secondary antibodies (anti-mouse [7076, CST] or anti-rabbit [7074, CST]) in Tris-buffered saline at room temperature for 1 h. The images were developed by chemiluminescence (GE Healthcare, Chalfont St. Giles, UK) in a dark room.

Immunofluorescence analysis

TDLNs and other tissues of interest were harvested, and tissue sections of 8-μm thickness were prepared with a cryostat. After incubation with 5% BSA for 1 h, the sections were incubated with primary antibody (anti-CD3, 1:500, Servicebio, China, GB13014; anti-Foxp3, 1:500, Servicebio, China, GB13445; anti-LYVE1, 1:100, Abcam, USA, Ab14917; anti-Ki67, 1:800, Servicebio, China, GB111141) overnight at 4°C in a wet, dark box. After being washed three times, the sections were incubated with the fluorescence-labeled secondary antibodies (CY3-goat anti-rabbit, 1:300, Servicebio, China, GB21303; 488-goat anti-rabbit, 1:300, Servicebio, China, GB25303) for 1 h at room temperature. Cell nuclei were counterstained with Hoechst33342. The sections were washed with PBS and then observed with a Nikon A1 Spectral Confocal Microscope (Nikon, Japan).

Exosome capture

Anti-OX40L (ab229021, Abcam), anti-CD62L (MA1-10262, Invitrogen), or control immunoglobulin G (IgG) was incubated with Protein A agarose beads (Pierce, Thermo Fisher). The exosome samples in PBS were further incubated with the above antibody-beads complex at room temperature for 1 h. The beads were then collected and washed two times with binding/wash buffer. To elute the exosomes, equal amounts of elution buffer (100 mM glycine·HCl, pH 2.5–3.0) were incubated with beads for 10 min at room temperature and the beads were cleared by centrifugation. Finally, the exosomes in the elution buffer were analyzed by NTA.

Flow cytometric analysis of immune cell populations

TDLNs and tumor tissue samples from mice with the indicated exosome treatments were collected and digested with collagenase type IV (1 mg/mL, Gibco, USA) in Hank's balanced salt solution (HBSS) containing calcium and magnesium for 2 h at 37°C. The cells were filtered through nylon mesh filters. The single-cell suspension was then diluted to a concentration of 1×10^7 cells/mL in culture medium. Prepared samples were then stained with anti-CD3-APC-Cy7, anti-CD4-BV421, anti-CD8-APC, and anti-Foxp3-PE. Cells were then washed twice with wash-cytometry buffer, followed by analysis with Beckman CytoFLEX. Flow cytometry data were analyzed by CytExpert software. Percentages of CTLs ($CD3^+CD4^-CD8^+$), helper T cells ($CD3^+CD4^+CD8^-$), and Tregs ($CD3^+CD4^+CD25^+Foxp3^+$) were calculated.

Histology

The mice were anesthetized and sacrificed after heart perfusion with saline and 4% paraformaldehyde (PFA). Lymph nodes were collected, fixed with 4% PFA, embedded in paraffin blocks, and sectioned at a thickness of 5 μm. The sections were stained with hematoxylin and eosin (H&E) to examine the lymph node metastases.

Statistical analysis

Data are expressed as mean ± SEM and were analyzed by one-way ANOVA for three-group comparison and log rank test for survival curves. Differences were considered significant at $p < 0.05$. All statistical analyses were conducted with GraphPad Prism 7.0.

SUPPLEMENTAL INFORMATION

Supplemental information can be found online at https://doi.org/10.1016/j.omtn.2021.10.009.

ACKNOWLEDGMENTS

This work was supported by grants from National Natural Science Foundation of China (81560431 to Q.L. and 81901027 to H.X.) and Natural Science Foundation of Guangxi (2020GXNSFAA259089 to Q.L.).

AUTHOR CONTRIBUTIONS

Conceptualization: methodology and writing, Q.L., G.Y., and H.X.; investigation, P.J, Z.Y., H.L., and M.W.; resources, Q.L., G.Y., and H.X.; funding acquisition, Q.L. and H.X.

DECLARATION OF INTERESTS

The authors declare no competing interests.

REFERENCES

1. Allemani, C., Matsuda, T., Di Carlo, V., Harewood, R., Matz, M., Nikšić, M., Bonaventure, A., Valkov, M., Johnson, C.J., Estève, J., et al.; CONCORD Working Group (2018). Global surveillance of trends in cancer survival 2000-14 (CONCORD-3): analysis of individual records for 37 513 025 patients diagnosed with one of 18 cancers from 322 population-based registries in 71 countries. Lancet *391*, 1023–1075.
2. Sung, H., Ferlay, J., Siegel, R.L., Laversanne, M., Soerjomataram, I., Jemal, A., and Bray, F. (2021). Global Cancer Statistics 2020: GLOBOCAN Estimates of Incidence and Mortality Worldwide for 36 Cancers in 185 Countries. CA Cancer J. Clin. *71*, 209–249.
3. Weigelt, B., Peterse, J.L., and van 't Veer, L.J. (2005). Breast cancer metastasis: markers and models. Nat. Rev. Cancer *5*, 591–602.
4. Meng, L., Liu, S., Liu, F., Sang, M., Ju, Y., Fan, X., Gu, L., Li, Z., Geng, C., and Sang, M. (2020). ZEB1-Mediated Transcriptional Upregulation of circWWC3 Promotes Breast Cancer Progression through Activating Ras Signaling Pathway. Mol. Ther. Nucleic Acids *22*, 124–137.
5. Núñez, N.G., Tosello Boari, J., Ramos, R.N., Richer, W., Cagnard, N., Anderfuhren, C.D., Niborski, L.L., Bigot, J., Meseure, D., De La Rochere, P., et al. (2020). Tumor invasion in draining lymph nodes is associated with Treg accumulation in breast cancer patients. Nat. Commun. *11*, 3272.
6. Stanton, S.E., and Disis, M.L. (2016). Clinical significance of tumor-infiltrating lymphocytes in breast cancer. J. Immunother. Cancer *4*, 59.
7. Kuerer, H.M., Newman, L.A., Buzdar, A.U., Hunt, K.K., Dhingra, K., Buchholz, T.A., Binkley, S.M., Ames, F.C., Feig, B.W., Ross, M.I., et al. (1998). Residual metastatic axillary lymph nodes following neoadjuvant chemotherapy predict disease-free survival in patients with locally advanced breast cancer. Am. J. Surg. *176*, 502–509.
8. Van Trappen, P.O., and Pepper, M.S. (2002). Lymphatic dissemination of tumour cells and the formation of micrometastases. Lancet Oncol. *3*, 44–52.
9. Munn, D.H., and Mellor, A.L. (2006). The tumor-draining lymph node as an immune-privileged site. Immunol. Rev. *213*, 146–158.
10. Hu, M., Yao, J., Cai, L., Bachman, K.E., van den Brûle, F., Velculescu, V., and Polyak, K. (2005). Distinct epigenetic changes in the stromal cells of breast cancers. Nat. Genet. *37*, 899–905.
11. Douglas, S.M., Bachelet, I., and Church, G.M. (2012). A logic-gated nanorobot for targeted transport of molecular payloads. Science *335*, 831–834.
12. Li, S., Jiang, Q., Liu, S., Zhang, Y., Tian, Y., Song, C., Wang, J., Zou, Y., Anderson, G.J., Han, J.Y., et al. (2018). A DNA nanorobot functions as a cancer therapeutic in response to a molecular trigger in vivo. Nat. Biotechnol. *36*, 258–264.
13. Jiang, Q., Liu, S., Liu, J., Wang, Z.G., and Ding, B. (2019). Rationally Designed DNA-Origami Nanomaterials for Drug Delivery In Vivo. Adv. Mater. *31*, e1804785.
14. Liu, S., Jiang, Q., Zhao, X., Zhao, R., Wang, Y., Wang, Y., Liu, J., Shang, Y., Zhao, S., Wu, T., et al. (2021). A DNA nanodevice-based vaccine for cancer immunotherapy. Nat. Mater. *20*, 421–430.
15. Kalluri, R., and LeBleu, V.S. (2020). The biology, function, and biomedical applications of exosomes. Science *367*, eaau6977.
16. Théry, C., Zitvogel, L., and Amigorena, S. (2002). Exosomes: composition, biogenesis and function. Nat. Rev. Immunol. *2*, 569–579.
17. Madeo, M., Colbert, P.L., Vermeer, D.W., Lucido, C.T., Cain, J.T., Vichaya, E.G., Grossberg, A.J., Muirhead, D., Rickel, A.P., Hong, Z., et al. (2018). Cancer exosomes induce tumor innervation. Nat. Commun. *9*, 4284.
18. Dong, Y., Lin, Y., Gao, X., Zhao, Y., Wan, Z., Wang, H., Wei, M., Chen, X., Qin, W., Yang, G., and Liu, L. (2019). Targeted blocking of miR328 lysosomal degradation with alkalized exosomes sensitizes the chronic leukemia cells to imatinib. Appl. Microbiol. Biotechnol. *103*, 9569–9582.
19. Yang, J., Wu, S., Hou, L., Zhu, D., Yin, S., Yang, G., and Wang, Y. (2020). Therapeutic Effects of Simultaneous Delivery of Nerve Growth Factor mRNA and Protein via Exosomes on Cerebral Ischemia. Mol. Ther. Nucleic Acids *21*, 512–522.
20. Bobrie, A., Colombo, M., Raposo, G., and Théry, C. (2011). Exosome secretion: molecular mechanisms and roles in immune responses. Traffic *12*, 1659–1668.
21. Li, Z., Zhou, X., Gao, X., Bai, D., Dong, Y., Sun, W., Zhao, L., Wei, M., Yang, X., Yang, G., and Yuan, L. (2020). Fusion protein engineered exosomes for targeted degradation of specific RNAs in lysosomes: a proof-of-concept study. J. Extracell. Vesicles *9*, 1816710.
22. Yang, J., Zhang, X., Chen, X., Wang, L., and Yang, G. (2017). Exosome Mediated Delivery of miR-124 Promotes Neurogenesis after Ischemia. Mol. Ther. Nucleic Acids *7*, 278–287.
23. Li, Z., Zhao, P., Zhang, Y., Wang, J., Wang, C., Liu, Y., Yang, G., and Yuan, L. (2021). Exosome-based *Ldlr* gene therapy for familial hypercholesterolemia in a mouse model. Theranostics *11*, 2953–2965.
24. Li, Z., Zhou, X., Wei, M., Gao, X., Zhao, L., Shi, R., Sun, W., Duan, Y., Yang, G., and Yuan, L. (2019). In Vitro and in Vivo RNA Inhibition by CD9-HuR Functionalized Exosomes Encapsulated with miRNA or CRISPR/dCas9. Nano Lett. *19*, 19–28.
25. Sun, W., Xing, C., Zhao, L., Zhao, P., Yang, G., and Yuan, L. (2020). Ultrasound Assisted Exosomal Delivery of Tissue Responsive mRNA for Enhanced Efficacy and Minimized Off-Target Effects. Mol. Ther. Nucleic Acids *20*, 558–567.
26. Demaria, M.C., Yeung, L., Peeters, R., Wee, J.L., Mihaljcic, M., Jones, E.L., Nasa, Z., Alderuccio, F., Hall, P., Smith, B.C., et al. (2020). Tetraspanin CD53 Promotes Lymphocyte Recirculation by Stabilizing L-Selectin Surface Expression. iScience *23*, 101104.
27. Croft, M., So, T., Duan, W., and Soroosh, P. (2009). The significance of OX40 and OX40L to T-cell biology and immune disease. Immunol. Rev. *229*, 173–191.
28. Webb, G.J., Hirschfield, G.M., and Lane, P.J. (2016). OX40, OX40L and Autoimmunity: a Comprehensive Review. Clin. Rev. Allergy Immunol. *50*, 312–332.
29. Zhang, X., Xiao, X., Lan, P., Li, J., Dou, Y., Chen, W., Ishii, N., Chen, S., Xia, B., Chen, K., et al. (2018). OX40 Costimulation Inhibits Foxp3 Expression and Treg Induction via BATF3-Dependent and Independent Mechanisms. Cell Rep. *24*, 607–618.
30. Fu, N., Xie, F., Sun, Z., and Wang, Q. (2021). The OX40/OX40L Axis Regulates T Follicular Helper Cell Differentiation: Implications for Autoimmune Diseases. Front. Immunol. *12*, 670637.
31. Cochran, A.J., Huang, R.R., Lee, J., Itakura, E., Leong, S.P., and Essner, R. (2006). Tumour-induced immune modulation of sentinel lymph nodes. Nat. Rev. Immunol. *6*, 659–670.
32. Oliver, G., and Alitalo, K. (2005). The lymphatic vasculature: recent progress and paradigms. Annu. Rev. Cell Dev. Biol. *21*, 457–483.
33. Wang, H., and Mooney, D.J. (2018). Biomaterial-assisted targeted modulation of immune cells in cancer treatment. Nat. Mater. *17*, 761–772.
34. Kuai, R., Ochyl, L.J., Bahjat, K.S., Schwendeman, A., and Moon, J.J. (2017). Designer vaccine nanodiscs for personalized cancer immunotherapy. Nat. Mater. *16*, 489–496.
35. Luo, M., Wang, H., Wang, Z., Cai, H., Lu, Z., Li, Y., Du, M., Huang, G., Wang, C., Chen, X., et al. (2017). A STING-activating nanovaccine for cancer immunotherapy. Nat. Nanotechnol. *12*, 648–654.
36. Tower, H., Ruppert, M., and Britt, K. (2019). The Immune Microenvironment of Breast Cancer Progression. Cancers (Basel) *11*, 1375.
37. Casey, S.C., Amedei, A., Aquilano, K., Azmi, A.S., Benencia, F., Bhakta, D., Bilsland, A.E., Boosani, C.S., Chen, S., Ciriolo, M.R., et al. (2015). Cancer prevention and therapy through the modulation of the tumor microenvironment. Semin. Cancer Biol. *35* (*Suppl*), S199–S223.
38. Egen, J.G., Kuhns, M.S., and Allison, J.P. (2002). CTLA-4: new insights into its biological function and use in tumor immunotherapy. Nat. Immunol. *3*, 611–618.
39. Sharpe, A.H., and Pauken, K.E. (2018). The diverse functions of the PD1 inhibitory pathway. Nat. Rev. Immunol. *18*, 153–167.

40. Van Allen, E.M., Miao, D., Schilling, B., Shukla, S.A., Blank, C., Zimmer, L., Sucker, A., Hillen, U., Foppen, M.H.G., Goldinger, S.M., et al. (2015). Genomic correlates of response to CTLA-4 blockade in metastatic melanoma. Science *350*, 207–211.

41. Maude, S.L., Frey, N., Shaw, P.A., Aplenc, R., Barrett, D.M., Bunin, N.J., Chew, A., Gonzalez, V.E., Zheng, Z., Lacey, S.F., et al. (2014). Chimeric antigen receptor T cells for sustained remissions in leukemia. N. Engl. J. Med. *371*, 1507–1517.

42. Ager, A., Watson, H.A., Wehenkel, S.C., and Mohammed, R.N. (2016). Homing to solid cancers: a vascular checkpoint in adoptive cell therapy using CAR T-cells. Biochem. Soc. Trans. *44*, 377–385.

43. Rosen, S.D. (2004). Ligands for L-selectin: homing, inflammation, and beyond. Annu. Rev. Immunol. *22*, 129–156.

44. Miyasaka, M., and Tanaka, T. (2004). Lymphocyte trafficking across high endothelial venules: dogmas and enigmas. Nat. Rev. Immunol. *4*, 360–370.

45. Girard, J.P., Moussion, C., and Förster, R. (2012). HEVs, lymphatics and homeostatic immune cell trafficking in lymph nodes. Nat. Rev. Immunol. *12*, 762–773.

46. Martinet, L., Garrido, I., Filleron, T., Le Guellec, S., Bellard, E., Fournie, J.J., Rochaix, P., and Girard, J.P. (2011). Human solid tumors contain high endothelial venules: association with T- and B-lymphocyte infiltration and favorable prognosis in breast cancer. Cancer Res. *71*, 5678–5687.

47. Ivetic, A. (2013). Signals regulating L-selectin-dependent leucocyte adhesion and transmigration. Int. J. Biochem. Cell Biol. *45*, 550–555.

48. Butcher, E.C., and Picker, L.J. (1996). Lymphocyte homing and homeostasis. Science *272*, 60–66.

49. Milutinovic, S., Abe, J., Godkin, A., Stein, J.V., and Gallimore, A. (2021). The Dual Role of High Endothelial Venules in Cancer Progression versus Immunity. Trends Cancer *7*, 214–225.

50. Weber, J.S., and Mulé, J.J. (2015). Cancer immunotherapy meets biomaterials. Nat. Biotechnol. *33*, 44–45.

51. Williams, C.A., Murray, S.E., Weinberg, A.D., and Parker, D.C. (2007). OX40-mediated differentiation to effector function requires IL-2 receptor signaling but not CD28, CD40, IL-12Rbeta2, or T-bet. J. Immunol. *178*, 7694–7702.

52. Ruby, C.E., Redmond, W.L., Haley, D., and Weinberg, A.D. (2007). Anti-OX40 stimulation in vivo enhances CD8+ memory T cell survival and significantly increases recall responses. Eur. J. Immunol. *37*, 157–166.

53. Rogers, P.R., Song, J., Gramaglia, I., Killeen, N., and Croft, M. (2001). OX40 promotes Bcl-xL and Bcl-2 expression and is essential for long-term survival of CD4 T cells. Immunity *15*, 445–455.

54. Song, J., So, T., Cheng, M., Tang, X., and Croft, M. (2005). Sustained survivin expression from OX40 costimulatory signals drives T cell clonal expansion. Immunity *22*, 621–631.

55. Walker, L.S., and Sansom, D.M. (2015). Confusing signals: recent progress in CTLA-4 biology. Trends Immunol. *36*, 63–70.

56. Gao, X., Ran, N., Dong, X., Zuo, B., Yang, R., Zhou, Q., Moulton, H.M., Seow, Y., and Yin, H. (2018). Anchor peptide captures, targets, and loads exosomes of diverse origins for diagnostics and therapy. Sci. Transl. Med. *10*, eaat0195.